First-principles study of bilayers ZnX and CdX (X = S, Se, Te) direct band-gap semiconductors and their van der Waals heterostructures

Gabriel Perin,[1,*] Danilo Kuritza,[1,†] Rafael Barbosa,[1,‡] Gustavo Tresco,[2,§] Renato B. Pontes,[3,‖] Roberto H. Miwa,[4,¶] and José E. Padilha[2,#]

[1]*Departamento de Física, Universidade Estadual de Maringá, 87020-900, Maringá, PR, Brazil*
[2]*Campus Avançado Jandaia do Sul, Universidade Federal do Paraná, 86900-000, Jandaia do Sul, PR, Brazil*
[3]*Instituto de Física, Universidade Federal de Goiás, Campus Samambaia, 74690-900, Goiânia, GO, Brazil*
[4]*Instituto de Física, Universidade Federal de Uberlândia, 38400-902, Uberlândia, MG, Brazil*

(Received 6 July 2023; accepted 5 October 2023; published 20 October 2023)

We conducted comprehensive first-principles investigations of the structural, electronic, and optical properties of hexagonal ZnX and CdX (X = S, Se, Te) and their van der Waals heterostructures. Our results indicate that all materials are thermally and dynamically stable, in contrast to earlier works. Electronic structure calculations with a hybrid functional revealed that the bilayers ZnX and CdX are characterized by a direct band gap (at the Γ point), primarily lies within the visible spectrum of the sunlight (with an exception for ZnS). Moreover, we found the band edges (VBM/CBM of the bilayers) lying below/above the oxidation/reduction potentials ($E^{O_2/H_2O}/E^{H^+/H_2}$) depending on the environment's pH. The effects of mechanical strain on the electronic properties of the bilayers have been thoroughly investigated, revealing an impressive tunability of the band gap, energy position of the band edges, and the ratio of the electron and hole effective masses. The calculated optical absorption spectra showed that the bilayers ZnX and CdX, with the exception of ZnS, absorb in the visible region. Besides that, we found exciton binding energies between 0.30 and 0.96 eV for ZnTe and CdS bilayers, confirming that the reduced screening effect in 2D systems leads to higher values of exciton binding energies. Furthermore, our results indicated that the ZnTe/CdS heterostructure exhibits a band gap within the visible sunlight spectra. The band edges are located in the bilayer ZnTe resulting in a type-I band offset. However, upon compressive strain, we verified the emergence of the type-II band alignment, as a result, the first absorption peak is redshifted and the exciton exciton wave function spreads out in both materials. Overall, our findings provide valuable insights into the potential of these materials for various technological applications in the fields of the photonics, photocatalysis, and optoelectronics.

DOI: 10.1103/PhysRevMaterials.7.104003

I. INTRODUCTION

The field of two-dimensional (2D) materials has been booming in recent years [1–3], following the discovery of graphene [4,5], a 2D monolayer of carbon, which presents fantastic properties, that could be applied in almost all areas of materials science and engineering [6–11]. The aforementioned 2D systems have been attracting great attention to the materials science community due to their unprecedent, unusual and unique physical-chemistry characteristics [1,2,12,13], that could be useful for many technological applications. Some classes of 2D materials include: transition metal dichalcogenides (TMDs), such as MoS2; hexagonal boron nitride (hBN), and black phosphorus (BP)[14]. TMDs, for instance, are semiconductors with a direct band gap, making them suitable for optoelectronics applications [15].

In addition to the dichalcogenides, we also have the monochalcogenide materials, composed by elements from groups II-IV of the periodic table. These include ZnX and CdX, with X being S, Se or Te. Such three-dimensional (3D) bulk structures can be found in nature in two possible crystal structures: wurtzite (WZ) and zinc blende (ZB). However, in recent years, 2D nanosheets of CdX with one through a few atomic layers have been synthesized from solvothermal and colloidal techniques [16–18]. The monolayer of CdX explored previously are equivalent to a cut along the (111) plane of the ZB phase or equivalently the (0001) plane of the WZ phase, which are found to relax to planar graphene-like honeycomb lattices. Similar 2D monolayer (ML) and bilayer (BL) hybrid structures of ZnX have also been reported [16,19,20]. Also, Sun Yongfu *et al.* [21] synthesized a single layer honeycomb lattice of ZnSe by exfoliating its lamellar hybrid intermediate followed by removing the alkylamine ligand with heating, they found that the photocurrent density 4–10 times higher than those of its ligand-coated hybrid layers, 8 times higher than quantum dots, and nearly 195 times higher than that of its bulk counterpart. Such experimental progress leads to

*gabriel_perin93@hotmail.com
†danilokuritza@gmail.com
‡barbosa90r@gmail.com
§tresco@ufpr.br
‖pontes@ufg.br
¶hiroki@ufu.br
#jose.padilha@ufpr.br

 ©2023 American Physical Society

envision the obtention of free-standing monolayer of CdX in a near future, which can offer a novel set of 2D layered materials for technological applications.

Besides that, 2D direct band gap semiconductors (such as theoretically and/or experimentally predicted for: CdX [22], ZnX [23,24], MoX_2 [25–27], WX_2 [26,28], among others [29–31]), have important applications due to their unique electronic and optical properties, including high energy gaps that cover the entire visible spectrum [32]. This makes them ideal for use in optoelectronic devices such as solar cells, photodetectors, and light-emitting diodes [33–36]. Additionally, they have recently gained attention for their potential use in photocatalysis, specifically in the generation of hydrogen via water splitting [37,38]. Their two-dimensional nature makes them promising candidates for next-generation electronic and energy devices with improved performance and energy efficiency, while their low formation energy (around 200 meV/atom) and ability to be exfoliated from their bulk and stabilized using suitable substrate (i.e., graphene) make them attractive for use in nanoelectronics and nanophotonics [39]. Thus the physical-chemistry properties of 2D direct band gap semiconductors make them promising materials for various applications in fields such as renewable energy, environmental science, and materials science.

In parallel, 2D van der Waals (vdW) heterostructures have emerged as an important class of materials due to their unique properties, which are derived from the combination of different 2D materials with complementary properties [14,40,41]. These heterostructures allow the creation of complex electronic and optoelectronic devices with unprecedented functionalities and performance [42]. Overall, the use of 2D van der Waals heterostructures holds great potential for a wide range of applications in various fields, including chemical sensing, electronics, photovoltaic, optoelectronics, catalysis, and energy storage [43–47]. For instance, by combining 2D direct band gap semiconductors like ZnX and CdX (X = S, Se, Te) with other 2D materials such as graphene, MoS_2, or C_2N, it is possible to create heterostructures with tailored band alignment and optical properties for photo/electro-catalyst applications [48–50]. However, as novel 2D materials, a systematic exploration of the electronic and optical properties of the bilayers ZnX and CdX and their vdW heterostructures is still quite important and essential.

With these motivations, herein we aim to explore, by performing first-principles calculations based on hybrid density functional theory, the structural, electronic, and optical properties of 2D bilayers ZnX and CdX and their vdW heterostructures. Our results show that these 2D materials possess direct band gaps, which are promising for applications in optoelectronics, including photovoltaics, photodetectors, and light-emitting diodes. Moreover, we have studied the electronic properties of vdW heterostructures composed of these 2D materials and we have found that they exhibit unique band alignment and electronic properties that can lead to novel device applications. Thus our study provide valuable insights into the properties of 2D ZnX and CdX materials and their heterostructures, which can guide future experimental studies and the design of new devices with improved performance.

II. METHODS

Our calculations were based on density functional theory, as implemented in the VASP code [51,52]. As conventional exchange correlation functionals underestimate the band gap of semiconductors, we used the hybrid functional of Heyd, Scuseria, and Ernzerhof (HSE06) [53,54], which gives more accurate band gaps and at the same time also accurate structural properties. The projector augmented wave potential (PAW) [55] was used to treat the ions-electrons interactions, and a plane wave cutoff energy of 400 eV was used to expand the valence electron wavefunctions (Zn: $3d^{10}4s^2$; Cd: $4d^{10}5s^2$; S: $3s^23p^4$; Se: $4s^24p^4$; Te: $5s^25p^4$). We used 20 Å of vacuum to avoid spurious interactions with the periodic images. The Brillouin zone is sampled with a $9 \times 9 \times 1$ k-point sampling. The vdW interactions are included by using the semiempirical D2 method [56] and together with HSE06 the lattice parameters and atomic positions for all structures are relaxed until residual forces on the atoms are smaller than 0.001 eV/Å. After the structural optimization, the mechanical and dynamic stability of the systems were determined by calculating the elastic constants using the VASPKIT code [57] and the phonon dispersion using PHONOPY code [58]. The thermal stability was verified by *ab initio* molecular dynamics simulations (AIMD) at 300 K, with a time step of 1 fs using Nosé heat bath scheme [59]. The valence-band (VB) and conduction-band (CB) edges with respect to the vacuum level are determined by aligning the planar-averaged electrostatic potential within the layer with the vacuum region. All calculations presented in main manuscript were conducted without spin-orbit coupling (SOC), however in Ref. [60], we present the results of the electronic structure with SOC.

In order to analyze the optical properties and the excitonic effects, we started with the Kohn-Sham orbitals of DFT calculation to obtain the self-energies G_0W_0. To avoid the screening problems in low dimensions, we truncate the Coulomb interaction along the perpendicular axis. In order to verify the e-h interaction, we solved the Bethe-Salpeter equation (BSE) [61–63] with the Tamm-Dancoff approximation [64]. The G_0W_0 and BSE calculations were performed with the YAMBO code [65]. We have been specially cautious to check the convergence of the number of k points, which we use a grid $32 \times 32 \times 1$ for bilayers and $20 \times 20 \times 1$ for bilayer CdS-ZnTe heterostructure.

III. RESULTS AND DISCUSSIONS

There are several structural proposals for 2D ZnX and CdX, with X = S, Se, and Te, based on the lattice (cleavage) plane orientations of their ZB or WZ parents [34,66]. In a seminal work, based on first-principles calculations, Zhou *et al.* predicted that the monolayer and bilayer hexagonal lattices, ZB111/WZ001, are dynamically unstable based on the phonon spectra calculations. In the same study, through molecular dynamics simulations, the authors verified the formation of corrugated structures in the hexagonal ML systems. Further investigations confirmed the presence of imaginary frequencies in hexagonal MLs CdX (X = S, Se, and Te) [39,67]. On the other hand, first-principles calculations, performed by Garg *et al.*, indicate that the hexagonal ML CdS is

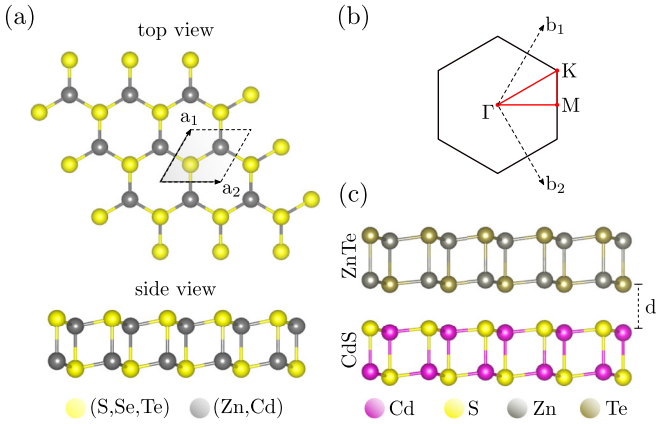

FIG. 1. (a) Ball-stick model of ZnX and CdX (X = S, Se, Te) (top and side views). The unit cell is represented by the shaded region in (a), defined by the vectors $\mathbf{a}_{1,2}$. (b) Schematic representation of the first Brillouin zone with the high-symmetry points highlighted. (c) Side view of the 2D vdW heterostructure of ZnTe/CdS.

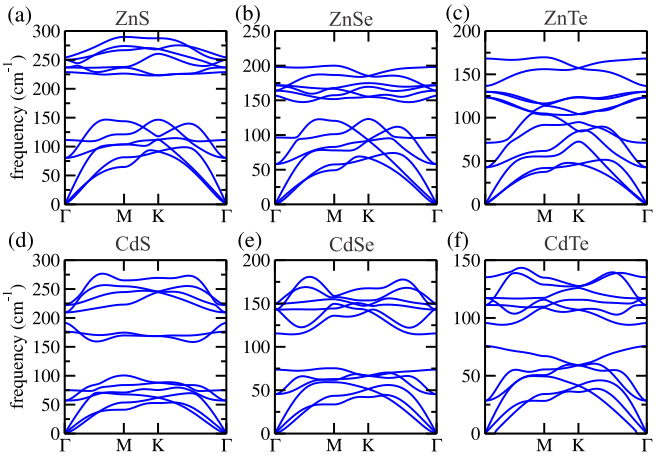

FIG. 2. Phonon dispersion curves for BLs: (a) ZnS, (b) ZnSe, (c) ZnTe, (d) CdS, (e) CdSe, and (f) CdTe.

not only energetically, but also dynamically, and structurally stable [68].

A. BLs ZnX and CdX

1. Structural stability

Let us start with the structural properties of hexagonal BL WZ001 systems ZnX and CdX, as depicted in Fig. 1(a). The hexagonal surface unit cell is represented by the shaded region, defined by the vectors $\mathbf{a}_1$ and $\mathbf{a}_2$. In Fig. 1(b), we present a schematic representation of the Brillouin zone with the high symmetry points considered in the band structure calculations. The equilibrium lattice constants, and other key structural parameters, like the elastic constants, are summarized in Table I. As we can observe, the lattice constant increases with the increase of the atomic radius of the chalcogen, showing that the structural parameters of the material are mainly governed by the chalcogen composition, ruled by the increase of the chalcogen atomic radius. It is worth noting that these systems present in-plane lattice constant close to the ones of the WZ bulk phases, thus indicating that the local atomic structures of the 3D bulk parents are somewhat preserved in the BL WZ001 systems.

TABLE I. Lattice parameters, nonzero components of the elastic constants, Young's modulus (Y_s) and Poisson's ratio (ν) of the bilayers ZnX and CdX. The lattice constant a is given in Å. The values of the elastic constants C_{11}, C_{22}, C_{66}, and the Young modulus Y_s are given in units of N/m.

System	a	C_{11}	C_{12}	C_{66}	Y_s	ν
ZnS	3.88	68.50	26.43	21.03	58.30	0.38
ZnSe	4.07	58.20	19.53	19.33	51.64	0.33
ZnTe	4.31	50.38	13.75	18.31	46.63	0.27
CdS	4.28	52.08	26.23	12.92	38.86	0.50
CdSe	4.41	39.92	17.62	11.15	32.14	0.44
CdTe	4.60	36.17	12.38	11.89	31.93	0.34
graphene [6]	2.46	352.7	60.9	145.9	342.2	0.17
h-BN [6]	2.50	289.8	63.7	113.1	275.8	0.22
silicene [6]	3.86	68.3	23.3	22.5	60.6	0.34

Based on the elastic constants are presented in Table I, we investigate the mechanical stability of the BL WZ001 ZnX and CdX materials through the calculation of the in-plane Young modulus, $Y_s = (C_{11}^2 - C_{12}^2)/C_{11}$, and the Poisson ratio, $\nu = C_{12}/C_{11}$. If one looks to the elastic constants of the materials, we find that $C_{11} = C_{22} > 0$, $C_{66} = \frac{1}{2}(C_{11} - C_{12}) > 0$, and $C_{11}C_{22} - C_{12}^2 > 0$, for all materials. Thus, accordingly with the Born criteria [69], we can infer that the WZ001 BLs ZnX and CdX are mechanically stable.

For the dynamical stability, based on the finite-displacement approach with supercell sizes of 4×4 primitive unit cells, we have calculated the phonon spectra of BLs ZnX and CdX. As shown in Figs. 2(a)–2(c) for ZnS, ZnSe, and ZnTe and Figs. 2(d)–2(f) for CdS, CdSe, and CdTe the phonon frequencies are all positives, except for a small imaginary pocket at Γ for CdTe. This imaginary pocket in the flexural phonon branch is very sensitive to details in the calculation and is a common issue in first-principles calculations for 2D materials, as was already pointed out by Fal'ko *et al.* [70]. In this way, our results indicate that those systems are dynamically stable. These findings are in contrast with those presented by Zhou *et al.* [34], where they found imaginary frequencies in BLs CdX, with X = S, Se, and Te. Here, it is worth noting that imaginary frequencies can be found in phonon calculations using (small) 2×2 and 3×3 supercells (see Fig. S8 in Ref. [60]).

The thermal stability of these BL systems was examined through *ab initio* molecular dynamics (AIMD) simulations. We have considered a simulation temperature of 300 K, with a time step of 1 fs using a Nosé heating bath scheme,[59] and a 4×4 surface supercell containing 16 formula units to minimize the constraint induced by the periodicity. The results of the variations of the total potential energy with respect to the simulation time and snapshots of the last configurations are presented in Figs. 3(a)–3(c) and 3(d)–3(f) for ZnX and CdX (with X = S, Se, and Te), respectively. As

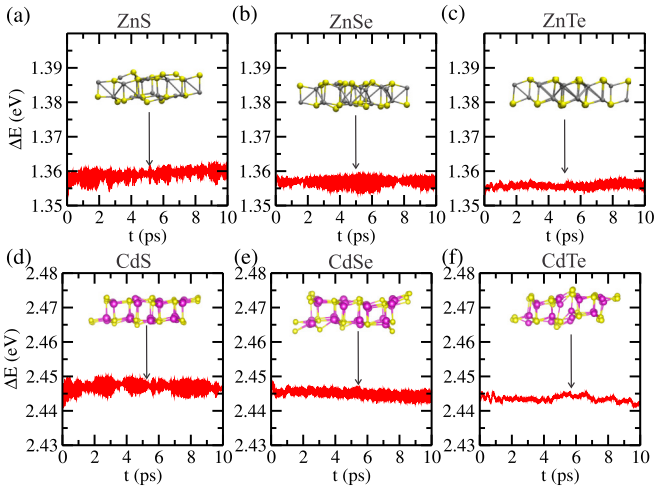

FIG. 3. Energy fluctuation curves for BLs: (a) ZnS, (b) ZnSe, (c) ZnTe, (d) CdS, (e) CdSe, and (f) CdTe. The temperature of the AIMD was set to 300 K. The insets show snapshots of the crystal structures at 10 ps (final configurations).

we can observe, the atomic configuration of the BLs remains nearly unaltered up to 10 ps and no phase transition is observed in the total potential energy. These results demonstrate that the WZ001 BLs ZnX and CdX, once synthesized, are stable and can preserve their structural integrity at room temperature.

TABLE II. Band gap, calculated effective mass of electron/hole and effective mass ratio (D), for all BLs considered. The band-gap values are given in eV.

System	E_g^{HSE06}	m_e^* (m_0)	m_h^* (m_0)	D
ZnS	3.994	0.22	−0.96	4.36
ZnSe	2.898	0.17	−0.99	5.82
ZnTe	1.786	0.12	−0.84	7.00
CdS	2.890	0.21	−0.93	4.42
CdSe	2.504	0.18	−0.98	5.44
CdTe	1.886	0.13	−0.91	7.00

2. *Electronic properties*

Once we have confirmed the mechanical, dynamical, and thermal stability of the bilayers ZnX and CdX WZ001, we will investigate the electronic properties of these systems, focusing on the key features for applications in photocatalytic water-splitting (WS) processes.

In Figs. 4(a1)–4(a6), we present the electronic band structures of BLs ZnX and CdX obtained by using hybrid functional within the HSE06 approach. These systems present direct band gaps at the Γ point, which is an advantage (in WS processes), since the optical transition process will occur without any loss due to phonons, and thus, increasing the light absorption rate. We find that the energy band gaps (E_g), presented in Table II, are (i) proportional to the electronegativity of the chalcogen atom, and (ii) inversely proportional to the

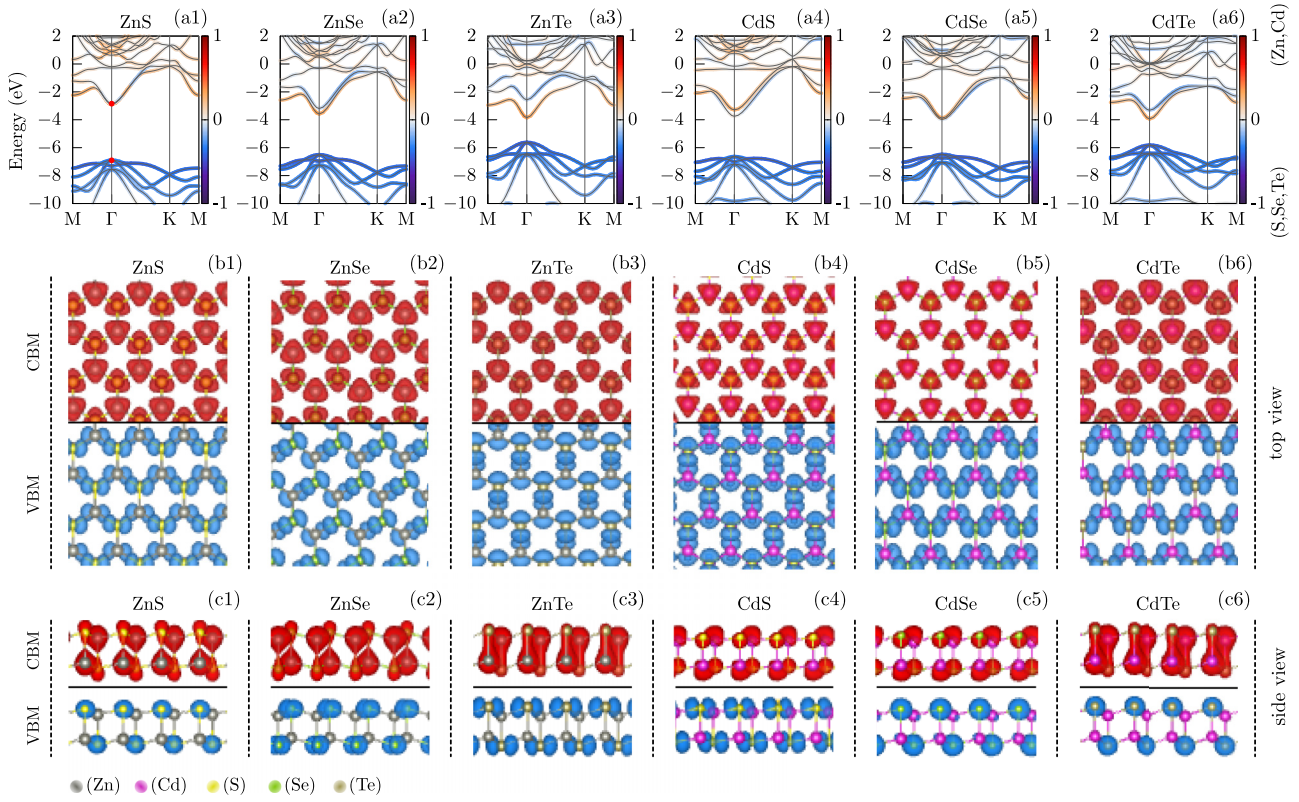

FIG. 4. [(a1)–(a6)] Band structure for BLs ZnX and CdX with atomic projections. All electronic band structures were aligned with respect to the vacuum level. [(b1)–(b6)] Top view of the VBM and CBM squared wave functions at Γ point. [(c1)–(c6)] Side view of the VBM and CBM squared wave functions at Γ point.

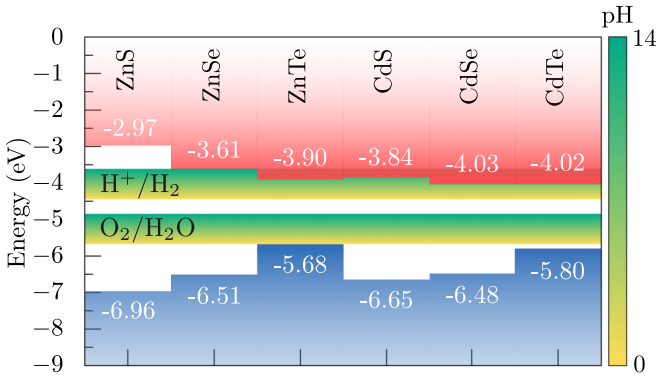

FIG. 5. Band edges for ZnX and CdX (X = S, Se, Te) bilayers aligned with respect to the vacuum level. We also present the reduction/oxidation potential of water as a function of the pH value (yellow to green region).

equilibrium constant of the BLs ZnX and CdX. Moreover, except for ZnS, E_g lie within the favorable range of the energy spectra for visible sunlight absorption, $E_g \lesssim 3$ eV. It is worth noting that similar values of band gaps were predicted for other structural phases of ZnX and CdX [34,66], for instance, E_g of 3.10, 2.97, and 2.90 eV in tetragonal MLs CdX (X = S, Se, and Te, respectively) [67]. In the same diagram, the color gradient represents the contribution of each atom in the composition of the energy bands, revealing that (i) the chalcogen atoms rule the formation of the valence band maximum (VBM) states, while (ii) the conduction band minimum (CBM) is composed by a superposition of the metal and chalcogen atoms. Further analysis of the squared wave functions at the Γ point reveals that the in-plane X-p_{xy} orbitals play a dominant role in shaping the valence-band maximum (VBM), extending across the surface layers of ZnX and CdX. Meanwhile, the conduction-band minimum (CBM) is primarily influenced by the hybridization between the s orbitals of the metal atoms, as depicted in Figs. 4(b1)–4(b6). This localized separation of photogenerated electrons (i) and holes (ii) suggests a reduction in the electron-hole recombination rate within the WZ001 BLs ZnX and CdX. See Ref. [60] for details regarding the orbital projections on the electronic band structure [60].

In addition to the electronic properties discussed above, it is necessary an appropriate alignment between the band-edges (CBM and VBM) of the photocatalytic material and the energy positions of the reduction and oxidation potentials, E^{H^+/H_2} and E^{O_2/H_2O}. The former (latter) should lie below (above) the CBM (VBM) of the photocatalytic material [66,71,72]. Moreover, it is worth noting that the reduction/oxidation potentials are related to the pH of water through, $E^{H^+/H_2} = (-4.44 + \text{pH} \times 0.059)$, and $E^{O_2/H_2O} = (-5.67 + \text{pH} \times 0.059)$ in eV [73]. That is, the photocatalysis process can be tuned by the pH of the chemical environment [74,75]. For instance, at pH=0, the reduction (oxidation) reaction will occur with the CBM (VBM) siting above (below) −4.44 (−5.67) eV with respect to the vacuum level.

Our results for the band edges of the BLs ZnX and CdX, and reduction/oxidation potentials as a function of the pH, indicated by the color gradient in Fig. 5, reveal that all BL systems ZnX and CdX can exhibit catalytic activity depending on the pH. For instance, BL ZnSe, which presents an energy gap ($E_g^{HSE06} = 2.9$ eV) suitable for sunlight absorption ($\leqslant 3$ eV), appears as a good candidate for WS processes over a wide range of hydrogen potential. The band edges for ZnX and CdX considering SOC can be found in Ref. [60], Fig. S3.

The effective mass (m^*) of electrons (e) and holes (h) (m_e^* and m_h^*, respectively) is an important feature that plays an important role on the efficiency of photocatalyst materials. Lower values of m_e^* and m_h^* not only decrease the e-h recombination rate, but also will improve the charge transfer process to the reactive sites. Our results of m_e^* and m_h^*, summarized in Table II, were obtained via quadratic fitting to the VBM and CBM at the Γ point of the BLs ZnX and CdX [76]. We find that m_e^* is proportional to the electronegativity of the chalcogen atom, and inversely proportional to the equilibrium constant. We found m_e^* between 0.12 and 0.22. In Ref. [77], the authors obtained $m_e^* = 0.16$, 0.11, and 0.08, for ZnX monolayer with X = S, Se, and Te. The reduced energy dispersion of the VBM results in larger values of hole effective masses in comparison with those obtained for electrons, m_e. We found m_h ranged between 0.84 and 0.99, Table II. In addition to the lower values of m^*, different values of the charge-carrier mobilities is an important feature in order to reduce the electron-hole recombination rate. Such a difference can be quantified by the ratio between the absolute values of the effective masses [71,76,78],

$$D = \frac{|m_h^*|}{|m_e^*|}. \tag{1}$$

Our results of D are summarized in Table II. A higher value of the relative ratio of the effective masses (D), indicates a large difference in the electron-hole mobility and thus reduces the recombination rate of electron-hole pairs. As we can see all ZnX and CdX BLs manifest higher values of D, between 4 and 7, which are comparable to other known photocatalysts [78]. Hence, we can infer that all BLs ZnX and CdX have lower electron-hole recombination rates, which enhances the photocatalytic water splitting efficiency.

3. *Strain effects*

Further control of the electronic properties of the 2D ZnX and CdX systems can be achieved through external mechanical strain. For instance, the metal-semiconductor transition in ML CdSe, and the tuning of the energy band gap in hexagonal ML CdS, and tetragonal CdX (with X = S, Se, and Te) [67,68,79].

Focusing on the key electronic features of BLs ZnX and CdX applied to the WS processes, we investigate the strain effects in the energy band gap (E_g); energy positions of the band edges of ZnX and CdX with respect to the redox potentials, E^{H^+/H_2} and E^{O_2/H_2O}; and the electron and hole effective masses (m_e^* and m_h^*). Our findings are summarized in Fig. 6.

As shown in Fig. 6(a), the energy gaps of BLs ZnX (with X = Se and Te) and CdX BLs (with X = S, Se, and Te) are suitable for visible light absorption, in general, characterized by a redshift (blueshift) upon tensile (compressive) strain, where the band edges present an energy downshift for $\varepsilon = -5\% \rightarrow +5\%$; with the CBM (VBM) crossing the pH

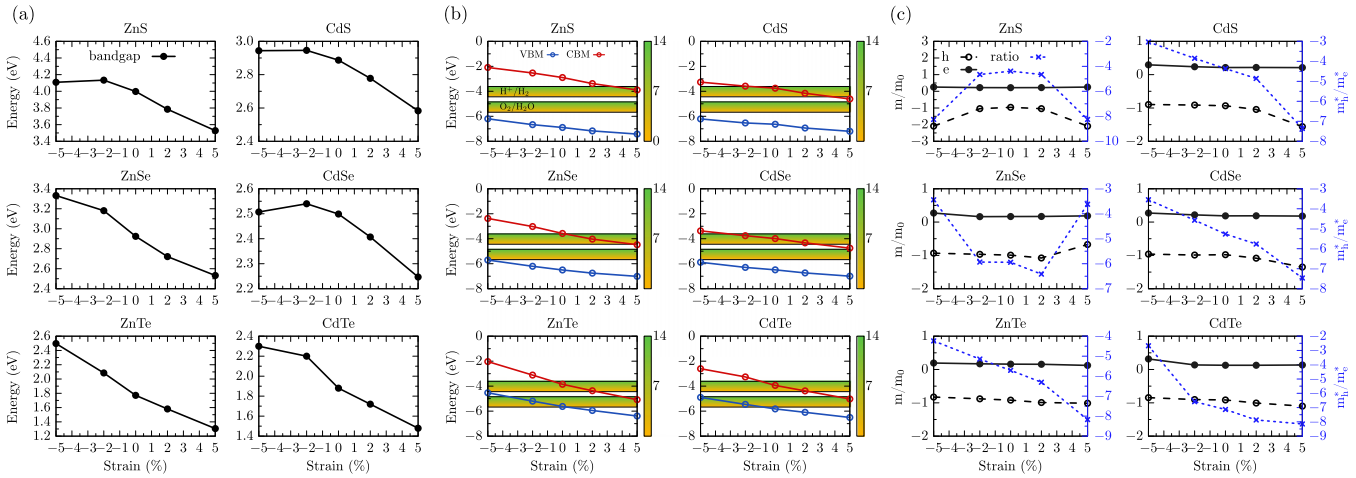

FIG. 6. For all ZnX and CdX investigated as a function of the strain: (a) variation of the electronic band gap. (b) VBM and CBM values aligned with respect to the vacuum level. The reduction/oxidation potential of water with respect to the pH value is also shown. (c) The DFT-calculated, effective mass of electron (m_e^*)/hole (m_h^*) and the ratio (m_h^*/m_e^*).

dependent reduction (oxidation) energy window for X = S, Se and Te (X = Te), Fig. 6(b). BL ZnTe is an exception, for ε between 2% and 6%. These results allow us to adjust the most suitable combination of strain and pH of the chemical environment for the water-splitting process. For instance, let us consider the BL ZnSe. The redox process will occur in ZnSe at the violet absorption spectra for ε between -5% and 0 (compressive strain) almost independently of the pH condition. Meanwhile, for ε about $+2\%$ (tensile strain), the absorption spectra lie in the blue-green region; however, the reduction process will be constrained to occur only for pH $\rightarrow$ 0. For $\varepsilon = +5\%$, the reduction process will stop since we find the CBM lying below the lower limit of the reduction potential, i.e., $E^{\mathrm{H^+/H_2}}$ for pH=0.

Once we have examined the strain effects on the band gap and band edges, we next examined the effect of mechanical strain on the electron and hole effective masses, m_e^*, and m_h^*. As shown in Fig. 6(c), we find that m_e^* is practically insensitive to the mechanical strain, while m_h changes by about 100% and 50% in BLs ZnS and CdS in comparison with the unstrained BLs, respectively. In ZnSe (CdSe) m_h reduces (increases) by less than 40% upon tensile strain, whereas in ZnTe and CdTe there is a slight increase of m_h for $\varepsilon \rightarrow +5$ %. These findings indicate that the changes in the hole effective mass mediated by the mechanical strain are mostly dictated by the chalcogen atoms. This is consistent with the predominant contribution of in-plane chalcogen-p_{xy} orbitals to the valence band edge states at the Γ point, as shown in Ref. [60], Figs. S9 and S10.

In the same diagram, we present the effective mass ratio, $D = m_e^*/m_h^*$, as a function of strain. We found that in ZnS and ZnSe BLs such an effective mass ratio is characterized by an essentially parabolic shape with the minimum (maximum) value of D in absolute values for $\varepsilon = 0$ (2%) in BL ZnS (ZnSe). In contrast, in CdX (X = S, Se, Te) and ZnTe BLs present a monotonic increase of D (in absolute values) upon tensile strain ($\varepsilon > 0$) up to 5%, which contributes to the reduction of the electron-hole recombination rate. We believe that these findings (summarized in Fig. 6) provide useful informations to guide the design of photocatalytic devices based on BLs WZ001 ZnX and CdX.

4. Optical properties

In addition to the key structural and electronic properties discussed above, in photocatalytic processes, the features of the optical absorption and excitons' binding energies are important issues that deserve to be examined. The optical absorption spectra are determined by the imaginary part of the macroscopic dielectric function (ϵ_2). In this study, ϵ_2 was calculated by using two different approaches, GW-RPA and -BSE (as described in the Sec. II), which will allow us to infer the role played by the e-h interaction (bound exciton states) in the absorption spectra.

In Fig. 7, we present the optical absorption spectra obtained by using GW-RPA and -BSE, indicated by the shaded regions and solid lines, respectively. Our findings clearly show that the e-h interactions significantly impact the optical absorption spectra of BLs ZnX and CdX, characterized by not only a redshift of the absorption edges [80] but also significant changes on the spectrum features. For instance, there is a noticeable and significant increase in the absorption intensity, as shown by the calculated oscillator strength (indicated by the solid purple lines in Fig. 7). It is worth noting that, with the exception of ZnS, all the other BLs ZnX and CdX present strong light absorption in the visible region, Fig. 7. In the BL ZnS, we find the first absorption peak at 3.94 eV in the GW-BSE calculation, which corresponds to the UV region. Meanwhile, the first absorption peak of the other BLs lies in the visible region, namely between 1.86 eV (BL CdTe) to 3.09 eV (BL ZnSe). These results demonstrate the potential of these 2D materials for various optical, photovoltaic, and photocatalytic applications. In Table III, we present the energies of the first absorption peaks, $E^{GW\text{-RPA}}$, $E^{GW\text{-BSE}}$, and the exciton biding energy (E^b), here defined as $E^b = E^{GW\text{-RPA}} - E^{GW\text{-BSE}}$ [81]. In general, due to the reduced screening, the exciton binding

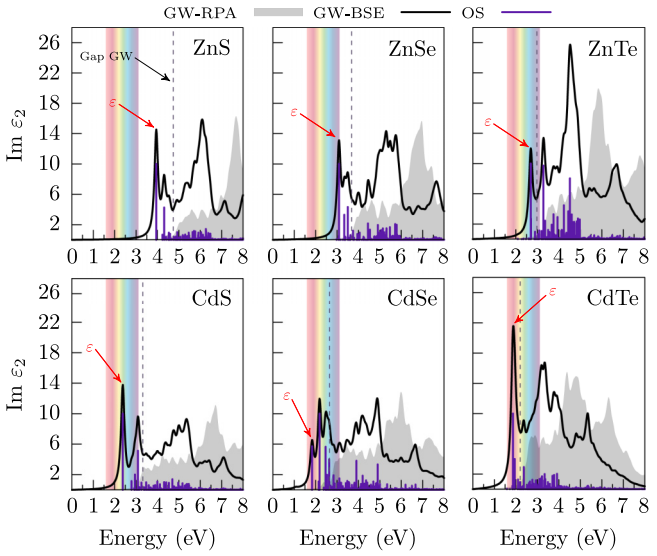

FIG. 7. Imaginary part of the dielectric function calculated with GW-RPA and GW-BSE of the pristine. The black dashed lines indicate GW band gap, the purple vertical lines indicate the oscillator strength and ϵ show the first exciton ($E^{GW\text{-BSE}}$).

energies in 2D systems are larger than that of their 3D counterparts [82].

Our results of E^b are comparable with the ones of other 2D materials with the presence of chalcogen atoms. For instance, we found $E^b = 0.80$ and 0.95 eV, for $X =$ S, BLs ZnS and CdS, which are close to those predicted for a single layer MoS_2 ($E^b = 0.96$ eV) [81] and MLs GeSe and SnTe (E^b of 0.88 and 0.95 eV, respectively) [83]. In addition to the dimensionality issues (e.g., 3D versus 2D), the width of the electronic band gap also contributes to the screening effects; in the BLs ZnX and CdX, the band gap is dictated by the electronegatity of the chalcogen atom. That is, there is a reduction of the band gap for X = S → Te, leading to an increase of the electronic screening[84], and thus a reduction of the exciton binding energy. Indeed, in ZnX (CdX), E^b reduces from 0.80 (0.96) to 0.30 eV (0.34 eV) for $X =$ S and Te, respectively. In particular, the exciton binding energies in BLs ZnS and CdS are comparable with those recently predicted for Janus MLs Ga_2STe and Gs_2SeTe, promising materials for photocatalysis [85].

TABLE III. Energies(GW-RPA and GW-BSE) and binding energies (in eV) of the first excitonic peak of the pristine BLs ZnX and CdX.

System	$E^{GW\text{-RPA}}$(eV)	$E^{GW\text{-BSE}}$ (eV)	E^b(eV)
ZnS	4.74	3.94	0.80
ZnSe	3.68	3.08	0.59
ZnTe	2.98	2.68	0.30
CdS	3.33	2.37	0.95
CdSe	2.65	1.82	0.82
CdTe	2.20	1.86	0.33

B. ZnTe/CdS vdW heterostructure

In photocatalyst processes, the electron-hole separation reduces the electron-hole recombination rate. Such a electron-hole separation takes place in Janus materials, mediated by an intrinsic electric field parallel to the stacking direction. In the ZnX and CdX BLs, such an electron-hole separation can be done by a suitable band alignment in vdW heterostructures. Here, we will focus on the ZnTe/CdS heterostructure, however, given the similarities in electronic properties among these materials, the results/analysis obtained/presented in this study can be extended to the other ZnX/CdX vdW heterostructures.

1. Structural and electronic properties

In Fig. 1(c), we present the structural model of ZnTe/CdS. The isolated BLs ZnTe and CdS present a lattice mismatch of ∼ 0.7%. In our calculations, we let the materials fully relax, i.e., atoms and lattice, resulting in minimal lattice mismatch and strain at the interface, about −0.5% for ZnTe and +0.2% for CdS. The energetic stability of the heterostructure was verified by the calculation of the interface binding energy, defined as the total energy difference between the final system, ZnTe/CdS heterostructure, and the sum of the total energies of the separated components, BLs ZnTe and ZnS, $\Delta E = E[\text{ZnTe/CdS}] - E[\text{ZnTe}] - E[\text{CdS}]$. We found $\Delta E = -18.34$ meV/Å^2 ($\Delta E = -36.47$ meV/Atom), which is comparable with other 2D vdW heterostructures, like bilayer graphene ($\Delta E = -50$ meV/Atom), and black phosphorus/graphene vdW heterostructure (−60 meV/Atom) [86]. At the equilibrium geometry, the vertical buckling of the BLs are preserved, and we find an interlayer distance of 3.56 Å suggesting the absence of interlayer chemical bonds.

The electronic band structure of the ZnTe/CdS heterostructure, at the equilibrium geometry, and the spatial localization of the valence-band maximum (VBM) and conduction-band minimum (CBM) at the Γ point are shown in Figs. 8(a3) and 8(b3), respectively. It is noticeable that the band structure of the heterostructure is practically a superposition of the energy bands of the separated BLs, namely, ZnTe and CdS, Figs. 4(a3) and 4(a4), respectively. Additionally, the band edge diagram, shown Fig. 5, suggests that ZnTe/CdS heterostructure will exhibit a type-I band alignment, with a sizable valence band offset (VBO) of ∼ 0.97 eV, and a small conduction band offset (CBO) of roughly 0.06 eV in Fig. 5. Indeed, this is what extract from the projected energy bands, Fig. 8(a3), namely, a type-I band alignment, with (i) the VBM and CBM localized in the BL ZnTe, (ii) VBO and CBO of 0.89 and 0.16 eV, and (iii) band gap of 1.89 eV, as schematically shown in Fig. 8(c3). Here, such a reduction (increase) of VBO (CBO) of about 0.1 eV, in comparison with the separated systems, can be attributed to the emergence of an electric dipole at the ZnTe/CdS interface.

2. Strain effects

As we have demonstrated previously, external strain can be used to tune the energy band gap, band edge positions, and the effective masses of BLs ZnX and CdX, Fig. 6. In this sense, our results of the evolution of the VBM and CBM, as a function of the external strain [Fig. 6(b)], allow us to infer that

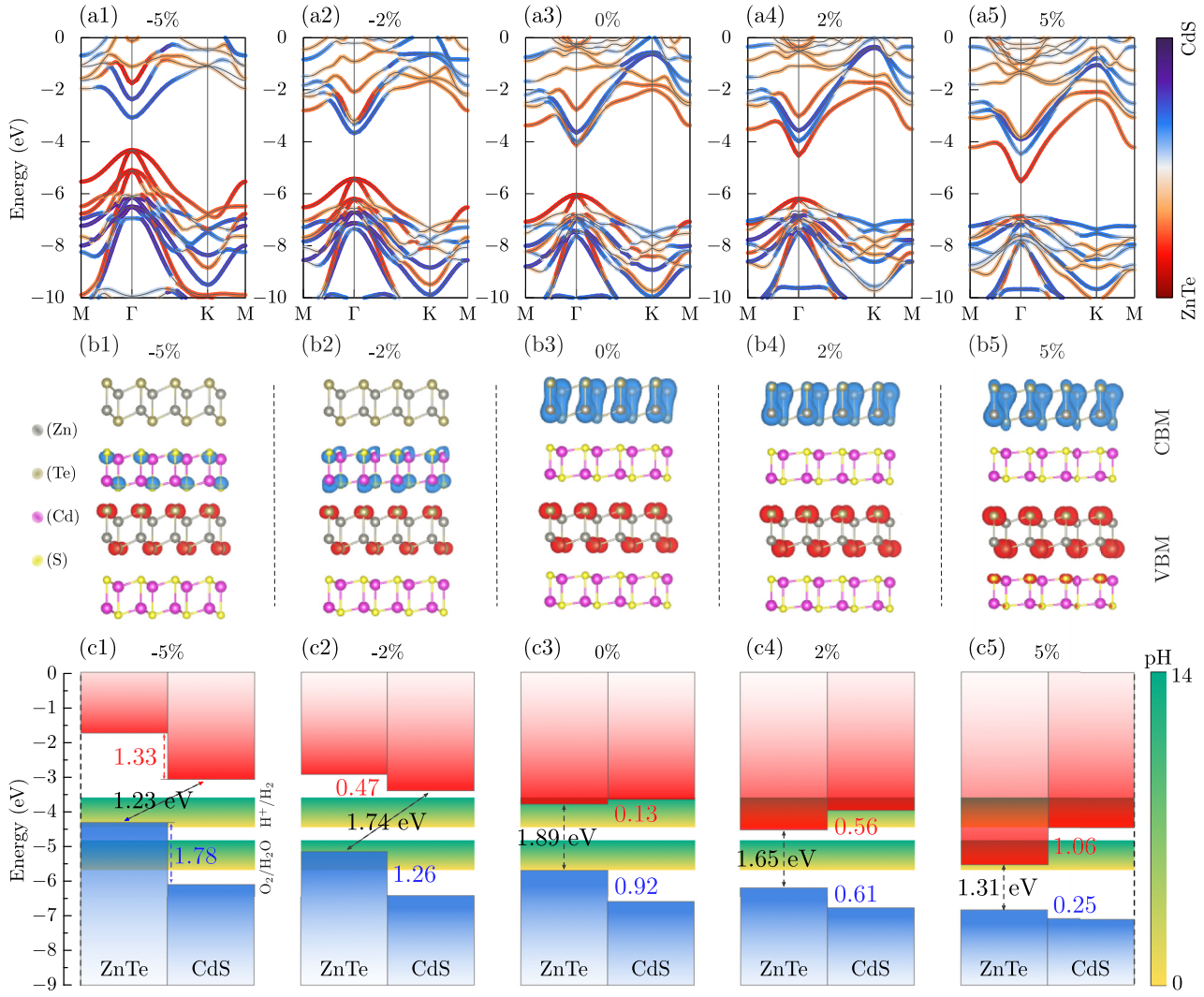

FIG. 8. As a function of the strain, for ZnTe/CdS heterostructure [(a1)–(a5] Band structures projected in their respective CdS and ZnTe layers with 0%, ±2%, and ±5% of strain. [(b1)–(b5)] Spatial localization of the valence-band maximum (VBM) and conduction-band minimum (CBM) at the Γ point. [(c1)–(c5)] Schematic representations of the band offsets (aligned with respect to the vacuum level) and the band gaps. We also present the reduction/oxidation potential of water with respect to the pH value.

in ZnTe/CdS heterostructures can present a strain-tuneable type-I ↔ type-II band alignment, namely, type-I band offset at the equilibrium and upon tensile strain ($\varepsilon \geqslant 0$), and type-II band offset for $\varepsilon < 0$, compressive strain. Indeed, this is what we find in the orbital projected electronic band structure of the ZnTe/CdS heterostructure [Figs. 8(a) and 8(b)], i.e., type-II band offset upon compressive strains of $\varepsilon = -5\%$ and -2%, and type-I band offset at the equilibrium geometry ($\varepsilon = 0$), and for tensile strains of $\varepsilon = +2\%$ and $+5\%$.

In Fig. 8(c), we show a schematic representation of the band offsets and the band gaps, of the ZnTe/CdS heterostructure, as a function of the strain. At the equilibrium geometry, $\varepsilon = 0$, the band edges lie on the ZnTe layer, type-I band offset, with the absorption spectra in the visible range. In this case, the oxidation and reduction processes will take place on the ZnTe side. On the other hand, it is noteworthy the emergence of type-II band offset upon slight compression of ZnTe/CdS heterostructure, giving rise to important features for the WS process. For instance, for $\varepsilon = -2\%$ [Fig. 8(c2)], the type-II band alignment leads to electron-hole separation, where the oxidation and reduction reactions will occur on the different sides of the heterostructure, namely, oxidation/reduction on the ZnTe/CdS sides. Additionally, the energy positions of the VBM/CBM of ZnTe/CdS with respect to $E^{O_2/H_2O}/E^{H_+/H_2}$ reveal that the oxidation will take place in a slightly alkaline environment, while the reduction process is not pH-restricted in the ZnTe/CdS heterostructures.

Finally, we examine the optical absorption spectra of ZnTe/CdS as a function of mechanical strain to provide a complete picture of the applicability of the ZnTe/CdS heterostructure as a potential material for photocatalysis. The absorption spectra of the ZnTe/CdS heterostructure, under different stress/strain conditions, are illustrated in Fig. 9(a). The spectrum without strain [$\varepsilon = 0$, Fig. 9(a2)] exhibits a peak at around 2.5 eV, which is close to the first absorption peak of the BL ZnTe, 2.6 eV. The real space exciton wave function (WF) shows that it is located solely in the ZnTe material [Fig. 9(b2)], which is a consequence of the type-I

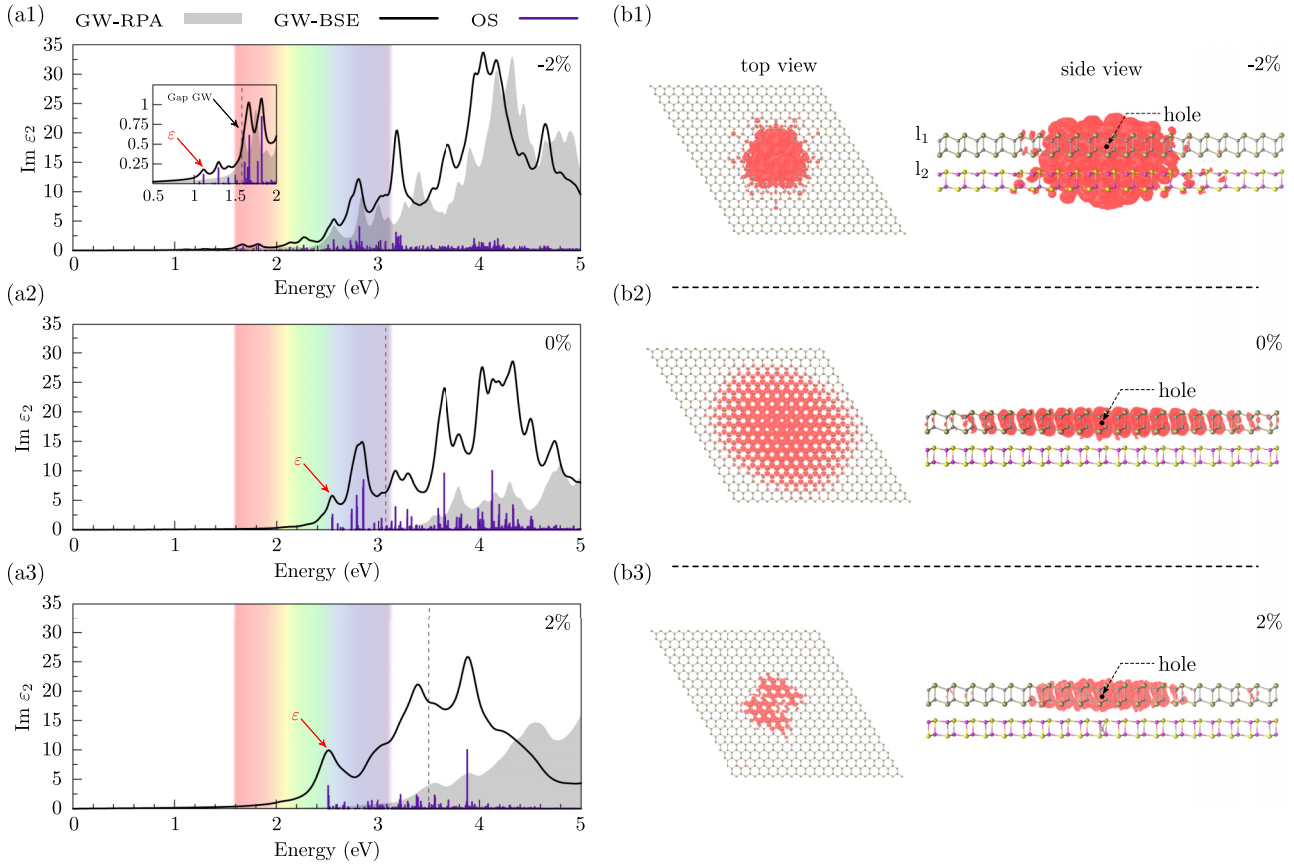

FIG. 9. Imaginary part of the dielectric function calculated with *GW*-RPA and *GW*-BSE of the bilayer CdS-ZnTe. The black dashed lines indicate GW band gap, the purple vertical lines are the oscillator strength and ϵ show the first exciton ($E^{GW\text{-BSE}}$). Normalized squared exciton wave function calculated using *GW*-BSE. The hole is located in the ZnTe layer. Bilayer ZnTe(l1) and CdS(l2) for (a) −2%, (b) 0%, and (c) 2%.

band offset, Fig. 8(c3). Upon a tensile strain of 2%, there are important changes in the absorption feature, followed by a modest red shift of the first exciton absorption peak, and the exciton WF remains located in the ZnTe material, Figs. 9(a3) and 9(b3). On the other hand, when a compressive strain of 2% is applied, the material's band alignment is changed, type-I → type-II [Fig. 8(c2)], as a result, the first absorption peak is redshifted to 1.1 eV [Fig. 9(a1)], and the exciton WF spreads out in both materials, as depicted in Fig. 9(b1).

In Table IV, we present the energies of the first absorption peak, $E^{GW\text{-RPA}}$ and $E^{GW\text{-BSE}}$, and the respective exciton binding energy, E^b. It is noticeable that (i) the energy position of the first optical absorption peak increases upon tensile strain, for instance, $E^{GW\text{-BSE}} = 1.11 \rightarrow 2.51$ eV, for $\varepsilon = -2\ \% \rightarrow +2\ \%$, as well as (ii) the exciton binding energy, $E^b = 0.47 \rightarrow 0.76$ eV, and (iii) the energy position of the bands edges (VBM and CBM) with respect to the vacuum level [Fig. 8(c)]. At the equilibrium geometry ($\varepsilon = 0$), we found E^b =0.51 eV, with the exciton WF localized in the ZnTe BL [Fig. 9(b2)], which is larger than the one obtained for the isolated ZnTe BL, 0.30 eV in Table III. The enhanced exciton binding energy in the ZnTe/CdS vdW heterostructure can be attributed to the significant enlargement of the energy gap that occurs upon the formation of the heterostructure. This gap increase, which is greater than the sum of the individual band gaps of the constituent layers, is a consequence of the interaction between the distinct layers within the system (see Fig. S7 in Ref. [60]). However, in addition to that, we can infer that the binding energies of the edge-states also contribute to the increase of E^b; as shown in Figs. 8(c2) → 8(c4), the binding energies of the VBM and CBM increases for $\varepsilon = -2\ \% \rightarrow +2\ \%$.

TABLE IV. Energies(*GW*-RPA and *GW*-BSE) and binding energies (in eV) of the first excitonic peak, with application of the strain in the CdS/ZnTe heterostructure.

Strain	$E^{GW\text{-RPA}}$(eV)	$E^{GW\text{-BSE}}$ (eV)	E_b(eV)
−2%	1.58	1.11	0.47
0%	3.06	2.55	0.51
2%	3.27	2.51	0.75

IV. SUMMARY AND CONCLUSIONS

We have carried out a theoretical investigation of bilayer systems Zn*X* and Cd*X* (with *X* = S, Se, and Te), and their counterpart ZnTe/Cd*X* vdW heterostructure using first-principles DFT calculations. We have focused on the applications in photocatalysis, particularly in the water-splitting process. Our findings reveal that, indeed, BLs Zn*X* and Cd*X* (with *X* = S, Se, and Te), with an exception for ZnS, and the combinations of these systems like ZnTe/CdS vdW

heterostructures present promising photocatalytic properties for the water-splitting process.

In contrast to earlier works, we find that both BLs ZnX and CdX are dynamically and structurally stable. Electronic structure calculations revealed that the BLs ZnX and CdX are characterized by direct band gap (at the Γ point), primarily lies within the visible spectrum of the sunlight (with an exception for ZnS). Moreover, we find the band edges (VBM/CBM of the BLs) lying below/above the oxidation/reduction potentials ($E^{O_2/H_2O}/E^{H^+/H_2}$) depending on the environment's pH. The effects of mechanical strain on the electronic properties of the BLs have been thoroughly investigated, revealing an impressive tunability of the band gap, energy position of the band edges, and the ratio (D) of the electron and hole effective masses. The calculated optical absorption spectra reveal that the BLs ZnX and CdX, with an exception of ZnS, absorb in the visible region. In consonance with previous works, we confirm that the reduced screening effect in 2D systems leads to higher values of exciton binding energies E^b. For instance, we found E^b between 0.30 and 0.96 eV for BLs ZnTe and CdS, respectively. Finally, based on the knowledge acquired in the BL systems, we have proposed vdW heterostructures through a combination of BLs ZnX and CdX. As a case study, we have considered the ZnTe/CdS vdW heterostructure.

The ZnTe/CdS heterostructure presents a band gap within the visible sunlight spectra; and band edges are located in the BL ZnTe, type-I band offset. Consequently, the oxidation and reduction reactions will take place on the ZnSe side. Upon compressive strain, we found the emergence of the type-II band alignment, resulting in (i) electron-hole separations, and (ii) oxidation/reduction reactions taking place at the different sides, i.e., ZnTe/CdS. Further optical absorption calculations confirm the emergence of absorption features within the visible range of sunlight, with an important contribution from electron-hole bound states, characterized by exciton binding energies between 0.47 and 0.76 eV for $\varepsilon = -2 \rightarrow +2\%$.

ACKNOWLEDGMENTS

This work was supported by the Brazilian agencies FAPEG, FAPEMIG, CNPq, and INCT/CNPq. We would like to acknowledge computing time provided by CENAPAD-SP and the National Laboratory for Scientific Computing (LNCC/MCTI) for providing HPC resources of the SDumont supercomputer.

[1] P. Miró, M. Audiffred, and T. Heine, Chem. Soc. Rev. **43**, 6537 (2014).
[2] S. Z. Butler, S. M. Hollen, L. Cao, Y. Cui, J. A. Gupta, H. R. Gutiérrez, T. F. Heinz, S. S. Hong, J. Huang, A. F. Ismach, E. Johnston-Halperin, M. Kuno, V. V. Plashnitsa, R. D. Robinson, R. S. Ruoff, S. Salahuddin, J. Shan, L. Shi, M. G. Spencer, M. Terrones *et al.*, and ACS Nano **7**, 2898 (2013).
[3] K. J. Koski and Y. Cui, ACS Nano **7**, 3739 (2013).
[4] K. S. Novoselov, A. K. Geim, S. V. Morozov, D. Jiang, Y. Zhang, S. V. Dubonos, I. V. Grigorieva, and A. A. Firsov, Science **306**, 666 (2004).
[5] A. K. Geim and K. S. Novoselov, Nat. Mater. **6**, 183 (2007).
[6] R. C. Andrew, R. E. Mapasha, A. M. Ukpong, and N. Chetty, Phys. Rev. B **85**, 125428 (2012).
[7] A. H. Castro Neto, F. Guinea, N. M. R. Peres, K. S. Novoselov, and A. K. Geim, Rev. Mod. Phys. **81**, 109 (2009).
[8] F. Schwierz, Nat. Nanotechnol. **5**, 487 (2010).
[9] A. K. Geim, Science **324**, 1530 (2009).
[10] X. Yu, H. Cheng, M. Zhang, Y. Zhao, L. Qu, and G. Shi, Nat. Rev. Mater. **2**, 17046 (2017).
[11] F. Bonaccorso, Z. Sun, T. Hasan, and A. C. Ferrari, Nat. Photonics **4**, 611 (2010).
[12] F. Schwierz, J. Pezoldt, and R. Granzner, Nanoscale **7**, 8261 (2015).
[13] K. Khan, A. K. Tareen, M. Aslam, R. Wang, Y. Zhang, A. Mahmood, Z. Ouyang, H. Zhang, and Z. Guo, J. Mater. Chem. C **8**, 387 (2020).
[14] K. S. Novoselov, A. Mishchenko, A. Carvalho, and A. H. C. Neto, Science **353**, aac9439 (2016).
[15] Q. H. Wang, K. Kalantar-Zadeh, A. Kis, J. N. Coleman, and M. S. Strano, Nat. Nanotechnol. **7**, 699 (2012).
[16] X. Huang and J. Li, J. Am. Chem. Soc. **129**, 3157 (2007).
[17] J. Son, X.-D. Wen, J. Joo, J. Chae, S.-i. Baek, K. Park, J. Kim, K. An, J. Yu, S. Kwon, S.-H. Choi, Z. Wang, Y.-W. Kim, Y. Kuk, R. Hoffmann, and T. Hyeon, Angew. Chem., Int. Ed. **48**, 6861 (2009).
[18] S. Ithurria, M. D. Tessier, B. Mahler, R. P. S. M. Lobo, B. Dubertret, and A. L. Efros, Nat. Mater. **10**, 936 (2011).
[19] X. Huang, J. Li, Y. Zhang, and A. Mascarenhas, J. Am. Chem. Soc. **125**, 7049 (2003).
[20] X. Huang, J. Li, and H. Fu, J. Am. Chem. Soc. **122**, 8789 (2000).
[21] Y. Sun, Z. Sun, S. Gao, H. Cheng, Q. Liu, J. Piao, T. Yao, C. Wu, S. Hu, S. Wei, and Y. Xie, Nat. Commun. **3**, 1057 (2012).
[22] J. Zhou, J. Huang, B. G. Sumpter, P. R. C. Kent, H. Terrones, and S. C. Smith, J. Phys. Chem. C **117**, 25817 (2013).
[23] J. Zhou, B. G. Sumpter, P. R. C. Kent, and J. Huang, ACS Appl. Mater. Interfaces **7**, 1458 (2015)
[24] P. D'Amico, A. Calzolari, A. Ruini, and A. Catellani, Sci. Rep. **7**, 16805 (2017).
[25] K. F. Mak, C. Lee, J. Hone, J. Shan, and T. F. Heinz, Phys. Rev. Lett. **105**, 136805 (2010).
[26] J. Gusakova, X. Wang, L. L. Shiau, A. Krivosheeva, V. Shaposhnikov, V. Borisenko, V. Gusakov, and B. K. Tay, Phys. Status Solidi (a) **214**, 1700218 (2017).
[27] S. Tongay, J. Zhou, C. Ataca, K. Lo, T. S. Matthews, J. Li, J. C. Grossman, and J. Wu, Nano Lett. **12**, 5576 (2012).
[28] W. Zhao, Z. Ghorannevis, L. Chu, M. Toh, C. Kloc, P.-H. Tan, and G. Eda, ACS Nano **7**, 791 (2013).
[29] S. Chabi and K. Kadel, Nanomaterials **10**, 2226 (2020).
[30] S. Zhang, S. Guo, Y. Huang, Z. Zhu, B. Cai, M. Xie, W. Zhou, and H. Zeng, 2D Mater. **4**, 015030 (2016).
[31] D. H. Ozbey, M. E. Kilic, and E. Durgun, Phys. Rev. Appl. **17**, 034043 (2022).
[32] A. Chaves, J. G. Azadani, H. Alsalman, D. R. da Costa, R. Frisenda, A. J. Chaves, S. H. Song, Y. D. Kim, D. He, J. Zhou, A. Castellanos-Gomez, F. M. Peeters, Z. Liu, C. L. Hinkle,

S.-H. Oh, P. D. Ye, S. J. Koester, Y. H. Lee, P. Avouris, X. Wang *et al.*, npj 2D Mater. Appl. **4**, 29 (2020).
[33] X. Zhang, B. Wang, X. Niu, Y. Li, Y. Chen, and J. Wang, Mater. Horiz. **5**, 1058 (2018).
[34] J. Zhou, J. Huang, B. G. Sumpter, P. R. Kent, Y. Xie, H. Terrones, and S. C. Smith, J. Phys. Chem. C **118**, 16236 (2014).
[35] D. Rai, S. Kaur, and S. Srivastava, Phys. B: Condens. Matter **531**, 90 (2018).
[36] S. Chen, F. Wu, Q. Li, H. Sun, J. Ding, C. Huang, and E. Kan, Nanoscale **12**, 15670 (2020).
[37] H. Verma, A. J. kale, C. Prakash, M. Harb, and A. Dixit, J. Electron. Mater. **50**, 7230 (2021).
[38] B. Wang, Y. Sun, and G. Yang, J. Phys. Chem. Lett. **13**, 190 (2022).
[39] J. Wang, J. Meng, Q. Li, and J. Yang, Phys. Chem. Chem. Phys. **18**, 17029 (2016).
[40] A. K. Geim and I. V. Grigorieva, Nature (London) **499**, 419 (2013).
[41] Y. Liu, N. O. Weiss, X. Duan, H.-C. Cheng, Y. Huang, and X. Duan, Nat. Rev. Mater. **1**, 16042 (2016).
[42] Y. Wen, P. He, Y. Yao, Y. Zhang, R. Cheng, L. Yin, N. Li, J. Li, J. Wang, Z. Wang, C. Liu, X. Fang, C. Jiang, Z. Wei, and J. He, Adv. Mater. **32**, 1906874 (2020).
[43] H.-L. Hou, C. Anichini, P. Samorì, A. Criado, and M. Prato, Adv. Funct. Mater. **32**, 2207065 (2022).
[44] C. Liu and P. Zhou, ACS Mater. Lett. **2**, 1101 (2020).
[45] S.-J. Liang, B. Cheng, X. Cui, and F. Miao, Adv. Mater. **32**, 1903800 (2020).
[46] T. Song, E. Anderson, M. W.-Y. Tu, K. Seyler, T. Taniguchi, K. Watanabe, M. A. McGuire, X. Li, T. Cao, D. Xiao, W. Yao, and X. Xu, Sci. Adv. **7**, eabg8094 (2021).
[47] I. Tantis, S. Talande, V. Tzitzios, G. Basina, V. Shrivastav, A. Bakandritsos, and R. Zboril, Adv. Funct. Mater. **33**, 2209360 (2023).
[48] Y. Zhang, J. Wei, T. Liu, Z. Zhong, Z. Luo, W. Xiao, B. Lv, X. Zhou, and X. Liu, Appl. Surf. Sci. **574**, 151679 (2022).
[49] J.-R. Zhang, Y.-Q. Zhao, L. Chen, S.-F. Yin, and M.-Q. Cai, Appl. Surf. Sci. **469**, 27 (2019).
[50] Y. Rao, F. Zhang, B. Zhu, H. Li, K. Zheng, Y. Zou, X. Feng, H. Guo, J. Qiu, X. Chen, and J. Yu, New J. Chem. **45**, 13571 (2021).
[51] G. Kresse and J. Furthmüller, Phys. Rev. B **54**, 11169 (1996).
[52] G. Kresse and J. Furthmüller, Comput. Mater. Sci. **6**, 15 (1996).
[53] J. Heyd, G. E. Scuseria, and M. Ernzerhof, J. Chem. Phys. **118**, 8207 (2003).
[54] J. Heyd, G. E. Scuseria, and M. Ernzerhof, J. Chem. Phys. **124**, 219906 (2006).
[55] G. Kresse and D. Joubert, Phys. Rev. B **59**, 1758 (1999).
[56] S. Grimme, J. Comput. Chem. **27**, 1787 (2006).
[57] V. Wang, N. Xu, J.-C. Liu, G. Tang, and W.-T. Geng, Comput. Phys. Commun. **267**, 108033 (2021).
[58] A. Togo, F. Oba, and I. Tanaka, Phys. Rev. B **78**, 134106 (2008).
[59] S. Nosé, J. Chem. Phys. **81**, 511 (1984).
[60] See Supplemental Material at http://link.aps.org/supplemental/10.1103/PhysRevMaterials.7.104003 for the electronic properties calculated with SOC, evolution of the band gap as a function of interlayer distance in the ZnTe and CdTe vdW heterostructure, phonon band structure as function of supercell size, and projected band structure for ZnX and CdX.
[61] G. Strinati, Phys. Rev. Lett. **49**, 1519 (1982).
[62] M. Rohlfing and S. G. Louie, Phys. Rev. B **62**, 4927 (2000).
[63] M. Palummo, O. Pulci, R. Del Sole, A. Marini, P. Hahn, W. G. Schmidt, and F. Bechstedt, J. Phys.: Condens. Matter **16**, S4313 (2004).
[64] S. Hirata and M. Head-Gordon, Chem. Phys. Lett. **314**, 291 (1999).
[65] A. Marini, C. Hogan, M. Grüning, and D. Varsano, Comput. Phys. Commun. **180**, 1392 (2009).
[66] J. Zhou, Adv. Theor. Simul. **2**, 1900061 (2019).
[67] M. Naseri, A. Bafekry, M. Faraji, D. Hoat, M. M. Fadlallah, M. Ghergherehchi, N. Sabbaghi, and D. Gogova, Phys. Chem. Chem. Phys. **23**, 12226 (2021).
[68] P. Garg, S. Kumar, I. Choudhuri, A. Mahata, and B. Pathak, J. Phys. Chem. C **120**, 7052 (2016).
[69] F. Mouhat and F.-X. Coudert, Phys. Rev. B **90**, 224104 (2014).
[70] V. Zólyomi, N. D. Drummond, and V. I. Fal'ko, Phys. Rev. B **89**, 205416 (2014).
[71] T. Le Bahers, M. Rerat, and P. Sautet, J. Phys. Chem. C **118**, 5997 (2014).
[72] A. K. Singh, K. Mathew, H. L. Zhuang, and R. G. Hennig, J. Phys. Chem. Lett. **6**, 1087 (2015).
[73] V. Chakrapani, J. C. Angus, A. B. Anderson, S. D. Wolter, B. R. Stoner, and G. U. Sumanasekera, Science **318**, 1424 (2007).
[74] L. G. Bloor, P. I. Molina, M. D. Symes, and L. Cronin, J. Am. Chem. Soc. **136**, 3304 (2014).
[75] K. Obata, R. van de Krol, M. Schwarze, R. Schomäcker, and F. F. Abdi, Energy Environ. Sci. **13**, 5104 (2020).
[76] M. Li, Y. Dai, W. Wei, and B. Huang, Phys. Chem. Chem. Phys. **20**, 9221 (2018).
[77] R. Chaurasiya, A. Dixit, and R. Pandey, J. Appl. Phys. **125**, 082540 (2019).
[78] M. Ashwin Kishore and P. Ravindran, J. Phys. Chem. C **121**, 22216 (2017).
[79] N. Chen, G. Yu, X. Gu, L. Chen, Y. Xie, F. Liu, F. Wang, X. Ye, and W. Shi, Chem. Phys. Lett. **595-596**, 91 (2014).
[80] M. Bernardi, M. Palummo, and J. C. Grossman, Phys. Rev. Lett. **108**, 226805 (2012).
[81] H. Guo, T. Yang, M. Yamamoto, L. Zhou, R. Ishikawa, K. Ueno, K. Tsukagoshi, Z. Zhang, M. S. Dresselhaus, and R. Saito, Phys. Rev. B **91**, 205415 (2015).
[82] A. Chernikov, T. C. Berkelbach, H. M. Hill, A. Rigosi, Y. Li, B. Aslan, D. R. Reichman, M. S. Hybertsen, and T. F. Heinz, Phys. Rev. Lett. **113**, 076802 (2014).
[83] R. Barbosa, D. Kuritza, G. Perin, R. H. Miwa, R. B. Pontes, and J. E. Padilha, Phys. Rev. Mater. **7**, 014001 (2023).
[84] R. Ravichandran, A. X. Wang, and J. F. Wager, Opt. Mater. (Amsterdam) **60**, 181 (2016).
[85] R. da Silva, R. Barbosa, R. R. Mancano, N. Duraes, R. B. Pontes, R. Miwa, A. Fazzio, and J. E. Padilha, ACS Appl. Nano Mater. **2**, 890 (2019).
[86] J. E. Padilha, A. Fazzio, and A. J. R. da Silva, Phys. Rev. Lett. **114**, 066803 (2015).